Geophysical Research Letters®

Key Points:

- Natural observations and numerical simulations of slow earthquakes share common average dynamical properties
- Natural observations show higher complexity than numerical simulations
- Matching instantaneous dynamical properties can help reducing the discrepancies between natural and simulated slow earthquakes

Correspondence to:

A. Gualandi,
ag2347@cam.ac.uk

Author Contributions:

Conceptualization: A. Gualandi, L. Dal Zilio
Data curation: A. Gualandi, L. Dal Zilio
Formal analysis: A. Gualandi
Software: A. Gualandi
Visualization: A. Gualandi
Writing – original draft: A. Gualandi
Writing – review & editing: L. Dal Zilio, D. Faranda, G. Mengaldo

Similarities and Differences Between Natural and Simulated Slow Earthquakes

A. Gualandi[1,2] [ID], L. Dal Zilio[3,4] [ID], D. Faranda[5,6,7] [ID], and G. Mengaldo[8,9]

[1]Department of Earth Sciences, University of Cambridge, Cambridge, UK, [2]Osservatorio Nazionale Terremoti, Istituto Nazionale di Geofisica e Vulcanologia, Rome, Italy, [3]Earth Observatory of Singapore, Nanyang Technological University, Singapore, Singapore, [4]Asian School of the Environment, Nanyang Technological University, Singapore, Singapore, [5]Laboratoire des Sciences du Climat et de l'Environnement, University of Paris-Saclay, Paris, France, [6]London Mathematical Laboratory, London, UK, [7]Laboratoire de Meteorologie Dynamique, Paris, France, [8]Department of Mechanical Engineering, National University of Singapore, Singapore, Singapore, [9]Honorary Research Fellow, Department of Aeronautics, Imperial College, London, UK

Abstract We investigate similarities and differences between natural and simulated slow earthquakes using nonlinear dynamical system tools. We use spatio-temporal slip potency rate data derived from Global Navigation Satellite System (GNSS) position time series in the Cascadia subduction zone and numerical simulations intended to reproduce their pulse-like behavior and scaling laws. We provide metrics to evaluate the accuracy of simulations in mimicking slow earthquake dynamics. We investigate the influence of spatio-temporal coarsening as well as observational noise. Despite the use of many degrees of freedom, numerical simulations display a surprisingly low average dimension, akin to natural slow earthquakes. Instantaneous dynamical indices can reach large values (>10) instead, and differences persist between numerical simulations and natural observations. We propose to use the suggested metrics as an additional tool to narrow the divergence between slow earthquake observations and dynamical simulations.

Plain Language Summary Earthquakes are natural phenomena resulting from the Earth's crust cyclically loading and unloading. The unpredictability of seismic events, combined with the large energy they release during the co-seismic phase, poses not only scientific challenges but also significant threats to numerous populated regions at risk. Numerical simulations of the seismic cycle are widely used to better understand the dynamics of this natural phenomenon. Nonetheless, a direct comparison of earthquake observations and numerical simulations of the seismic cycle is currently prevented by the lengthy recurrence time of large seismic events rupturing the same fault segment and the short observational record at our disposal. Slow earthquakes, exhibiting lower recurrence times, serve as a viable alternative for validating models against real-world observations. We investigate similarities and differences between natural and simulated slow earthquakes through the lens of nonlinear dynamical system theory. We study the effects of observational noise and spatio-temporal coarsening putting the simulations in conditions like real-world observations. We find that observational noise does not suffice to explain the higher complexity retrieved for natural observations. By refining our understanding of these dynamical systems, this study contributes to advancements in seismic research, offering a picture of the complexities involved on active faults.

1. Introduction

The Earth's crust is complex and with many degrees of freedom (dof) active at different spatio-temporal scales (Ben-Zion, 2008). On the one hand, it has been proposed that the complexity manifested by earthquakes is due to the natural tendency of the Earth's crust toward a self-organized or near-critical state with infinite dof (Bak & Tang, 1989; Main, 1996). On the other hand, infinite dof may result from a continuum representation of the Earth's crust, but fault segmentation is commonly observed at plate boundaries (Philibosian & Meltzner, 2020), and the aperiodicity of earthquake recurrence can be interpreted as the result of low-dimensional chaotic behavior (Becker, 2000; Huang & Turcotte, 1990; McCloskey & Bean, 1992).

Being able to measure how many effective dof are active in a system is key to set up an appropriate model to describe it. Several data-driven techniques to measure the number of dof in the absence of explicit governing equations exist (Cao, 1997; Faranda, Messori, & Yiou, 2017; Grassberger & Procaccia, 1983; Sano & Sawada, 1985). To apply them, two major requirements must be satisfied: (a) we need sufficiently long time

series, to observe the attractor in many regions of the phase space; (b) we need a sufficient sampling rate, with at least a handful of samples to cover dynamical features (e.g., instabilities) of interest. Regular earthquakes typically exhibit long recurrence times ranging from several decades to millennia. For this reason, laboratory analogs (Leeman et al., 2018; Rosenau et al., 2017; Tinti et al., 2016) or numerical simulations (Cattania, 2019; Dal Zilio et al., 2019; Lapusta & Liu, 2009) are extensively used to study the seismic cycle. A direct comparison with the earthquake cycle in nature has been so far prevented because of the paucity of instrumental observations of recurring events rupturing the same fault segment. It follows that the available observations for regular earthquakes typically fail to fulfill the first requirement mentioned above. To overcome this issue at natural scale, slow slip events (SSEs), here referred also as slow earthquakes, provide an optimal focus, exhibiting parallels to regular earthquakes but with abbreviated recurrence times, approximately months or years, overcoming the observational limitations of the latter (Schwartz & Rokosky, 2007). SSEs are not as destructive as regular earthquakes but can reach magnitudes larger than seven and perturb the stress field in the surrounding of active faults (Radiguet et al., 2012). The actual role of SSEs in seismic hazard estimation has not been fully investigated yet, but stress perturbations induced by SSEs can potentially trigger large earthquakes (Radiguet et al., 2016), and they may be used to improve the estimate of time-dependent earthquake probabilities (Gomberg et al., 2005; Voss et al., 2018).

We use state-of-the-art spatio-temporal slip rate solutions relative to the Cascadia subduction zone (Michel et al., 2019a) and numerical simulations designed to mimic the natural behavior (Dal Zilio et al., 2020). A characterization of dynamical properties from kinematic solutions in Cascadia is already available (Gualandi, Avouac, et al., 2020). Here we want to characterize the data generated by numerical simulations and compare these results with those derived from real-world data analyses. Our study aims to provide insights to the earthquake modeling community to validate simulations against natural SSEs.

We apply metrics and complexity measures deduced from nonlinear dynamical system theory to both simulated and natural slow earthquake data. In particular, we estimate and compare the values of the local dimension d_1 (Faranda, Messori, & Yiou, 2017), of the local extremal index θ (Faranda, Messori, & Yiou, 2017), of the maximum Lyapunov exponent $\lambda_{\max}$ (Parlitz, 2016; Wolf et al., 1985), and of the spectral entropy H_{sp} (Llanos et al., 2017) (see Section S1 in Supporting Information S1). Our results suggest that natural slow earthquakes exhibit more complex and less predictable behaviors compared to those modeled by our state-of-the-art numerical simulations, but both are characterized by a low (<5) average dimension. Our findings underscore a discrepancy between the dynamic complexities inherent in natural slow earthquake behaviors and the predictions from current deterministic models of fault slip. To bridge this gap and enhance the accuracy of physics-based models, we call for the integration of both asymptotic and time-dependent (or local) dynamical metrics into the evaluation processes of numerical simulations. This enhancement will steer slow earthquake modeling toward improved accuracy, potentially fostering advancements in effective slow earthquake forecasting. We further indicate possible directions to reconcile the opposite views of low-dimensional chaos and self-organized criticality (SOC).

2. Data

All data used in this study are publicly available. For natural slow earthquakes, we use the slip potency p, equal to the product between the area that slipped and the amount of slip, derived from the daily position time series of 352 GNSS stations in Cascadia, spanning the time range 2007.0–2017.632 (Michel et al., 2019a). The Cascadia megathrust exhibits a distinctive slow-slipping belt at a depth of approximately 30–40 km. Gualandi, Avouac, et al. (2020) used the segmentation proposed by Michel et al. (2019b) and estimated nonlinear dynamical indices for each slipping segment from the slip potency rate $\dot{p}$. Their results suggest that the northern segments show a dynamics that is not ascribable to a pure stochastic process.

Dal Zilio et al. (2020) conducted numerical simulations on a planar fault governed by rate- and state-dependent friction (Dieterich, 1979; Ruina, 1983). The central section of the simulated fault, spanning approximately 300 km, features a frictionally unstable velocity weakening zone embedded within a loading section of frictionally stable rate-strengthening zone creeping at 40 mm/yr. This loading rate parallels that of Cascadia, and the size of the fault corresponds to the northernmost segment of Cascadia, extending roughly from latitude 47° northwards. The model is based on a set of Partial Differential Equations (PDE) with five dynamical variables: slip velocity, shear stress, rate- and state-friction state variable, pore pressure, and fault zone dilation (Segall & Rice, 1995). The values used for the model parameters can be found in Table S1 of Dal Zilio et al. (2020).

Theoretically, a system governed by PDEs represents a continuum system, and as such should have an infinite number of dof. However, numerical solutions for PDEs necessitate discretization, effectively resulting in a solution for a large coupled Ordinary Differential Equations (ODE) system. Accordingly, the expected maximum number of dof equates to the product of the number of patches used for fault discretization and the count of variables essential for comprehensive system characterization (five in this context). To align with the geodetic inversion size of a dense GNSS network, we downsampled the results of our model to 2.5×2.5 km^2 (e.g., Gualandi et al., 2017; Johanson et al., 2006). The model itself utilizes a resolution of 250 m to properly resolve the nucleation size (Rice & Ruina, 1983) and the cohesive zone size (Day et al., 2005). Similarly, we utilized an adaptive time-stepping to capture both long- and short-term processes (Lapusta et al., 2000). Subsequently, we downsampled the temporal resolution to daily sampled data, commonly used in the study of SSEs around the world (e.g., Kano et al., 2018, and references therein). While the simulations were executed at finer spatio-temporal resolutions, our modifications emulate observations in real-case scenarios. Given the spatial and temporal modifications, the simulated data comprise a spatial grid of 2,560 patches, with 928 in velocity-weakening regions, amounting to 56,826 time snapshots, equivalent to over 150 years. Similar to Cascadia, we limit our analysis to the slow slipping velocity weakening region. As a consequence, we might expect a number of dof as high as $928 \times 5 = 4,640$.

Some noticeable differences about fault geometry, inter-event times and adopted observable for the analysis emerge after a first visual investigation, and are reported in Section S2 in Supporting Information S1. Here we notice that the slip potency rate, that is, the time derivative of the slip potency p, for numerical simulations spans several orders of magnitude, and a natural way to study it is to analyze its Log_{10} value. Furthermore, the numerical simulations use as variable the logarithm of the slip velocity, making it a suitable variable to compare observed and simulated data. In the following we are going to show the results obtained studying the time series of the variable $\zeta = \text{Log}_{10}(\dot{p})$ for both data sets. In Figure 1 we show in map view the maximum value of ζ for each patch (panels a and b), and the time evolution of ζ integrated over the whole slipping area (panels c and d). Figure S1 in Supporting Information S1 shows the same but for $\dot{p}$ instead of ζ. To avoid unphysical backslip, a variation regularization filter (Chartrand, 2011) is adopted when dealing with data corrupted by observational noise (see Section S3 and Figure S2 in Supporting Information S1). In Figures S3 and S4 in Supporting Information S1 we show the power spectrum of the time series reported in panels c and d of Figure 1.

3. Results

3.1. Local Dynamical Metrics d_1 and θ

Figure 2 shows the local dynamical indices d_1 and θ. All panels are color coded using the value taken by the variable ζ at a given time t integrated over the whole slipping area. To ensure an estimate for the extremal index, we have chosen a quantile threshold starting from 0.99 and decreased it by 0.01 until at least one of the neighbors is not temporally adjacent to the current configuration under exam. Table S1 in Supporting Information S1 summarizes the quantile threshold for all the considered cases. The local indices for numerical simulations tend to be smaller than those for natural slow earthquakes. In particular, we find that the maximum dimension takes values $\max\{d_1^{\text{sse}}\} \sim 30$ versus $\max\{d_1^{\text{sim}}\} \sim 13$, the average dimension (or information dimension D_1) is $D_1^{\text{sse}} \sim 3.1$ versus $D_1^{\text{sim}} \sim 2.3$, and the extremal index ranges are $\theta^{\text{sse}} \in [0.009, 0.12]$ versus $\theta^{\text{sim}} \in [0.0002, 0.0042]$. Adding observational noise to the numerical simulations and filtering them leads to the following values: $\max\{d_1^{\text{sim noisy}}\} \sim 12$, $D_1^{\text{sim noisy}} \sim 4.2$, and $\theta^{\text{sim noisy}} \in [0.0004, 0.05]$ (Figure S5 in Supporting Information S1). The retrieved attractor dimension is on average small (<5). The instantaneous dimension highly depends on the selected variable for numerical simulations. In fact, $\max\{d_1^{\text{sim}}\} \sim 13$ when using ζ as variable (Figure 2), but it reaches 3,455 when using the slip potency rate $\dot{p}$ (Figure S5 in Supporting Information S1). Considering that we have used 928 patches, and each is described by five variables, when using $\dot{p}$ there are some regions in the phase space that are sensitive to almost all possible degrees of freedom, meaning that the information at almost each patch is needed to characterize the system in that moment in time. This is not the case for natural slow earthquakes, for which $\max\{d_1^{\text{sse}}\} \sim 30$ if we use either ζ or $\dot{p}$ (Figure S6 in Supporting Information S1). This is a consequence of the much larger range spanned by $\dot{p}$ for numerical simulations with respect to natural events, consistent with the differences visually noted before the analysis. The average dimension is less affected, going from $D_1^{\text{sim}}(\zeta) \sim 2.3$ to $D_1^{\text{sim}}(\dot{p}) \sim 5.2$. It follows that numerical simulations seem to have a smaller or larger
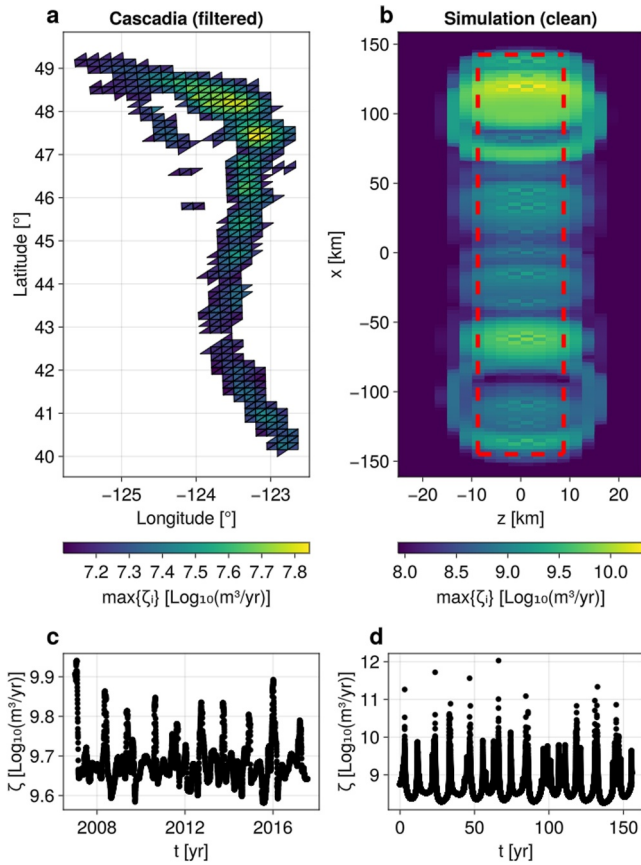
Figure 1. (a) Cascadia slow slipping belt, color coded by the Log_{10} of the maximum slip potency rate. (b) Same as (a), but for the simulation fault. The red dashed line indicates the velocity-weakening region here considered as comparison with the slipping belt in Cascadia. (c) Slip potency rate time series, obtained after integrating over the whole Casacadia slipping belt of panel (a). (d) Slip potency rate time series, obtained after integrating over the whole velocity-weakening area in panel (b). Note the necessity to use logarithmic scale for slip potency rates in the simulations to avoid saturation.

dimension with respect to natural SSEs ($D_1^{\text{sse}}(\zeta) \sim 3.1$, and $D_1^{\text{sse}}(\dot{p}) \sim 3.2$) depending on the variable considered. The noise and filter do not substantially affect the local dimension when using ζ as input variable, but they increase the estimates of θ by one order of magnitude. Using ζ seems natural because equations are integrated using this as a variable rather than the slip rate, and for this reason these are the results shown in the main text.

Figure 3 reports the values of normalized cross-correlation between the local indices time series and ζ integrated over the whole area considered for the analysis. We notice that d_1 for natural slow earthquakes correlates with ζ with two peaks, indicating a time-lag that precedes and follows ζ. This result is in agreement with (Gualandi, Avouac, et al., 2020), that studied individual slipping segments for natural events, meaning that d_1 tends to reach high values when a slow earthquake starts or ends. We notice that d_1 for natural slow earthquakes correlates with ζ with two peaks, indicating a time-lag that precedes and follows ζ. This result is in agreement with (Gualandi, Avouac, et al., 2020), that studied individual slipping segments for natural events, meaning that d_1 tends to reach high values when a slow earthquake starts or ends. θ instead shows a local peak that precedes the zero time-lag, but the results are noisier, with a global peak occurring at larger time delays. The cross-correlations for the numerical simulations show a single peak at almost zero time-lag instead. The cross-correlation is higher than for natural slow earthquakes, but it reduces to similar values when studying noisy (and filtered) time series. The filter makes the cross-correlation plots more spread. For the local dimension we can still identify a peak with slightly positive time-lag, but for the local extremal index the cross-correlation is highly corrupted (Figure S7 in Supporting Information S1). The variable $\dot{p}$ seems less sensitive to the filtering procedure (Figures S7 and S8 in Supporting Information S1). Results for Cascadia are similar, independently of the chosen variable (Figure S8 in Supporting Information S1).

The double versus single peak observed in the cross-correlation plots has immediate implications in terms of $d_1 - \theta$ space readability. Both the $d_1 - \theta$ plots in Figure 2 exhibit a clustering of blue points in the bottom left area of the plot, indicative of inter-SSE periods. Similarly, they also exhibit a clustering of yellow points on the top right area of the plot. The clustering is much more visible for simulated data than n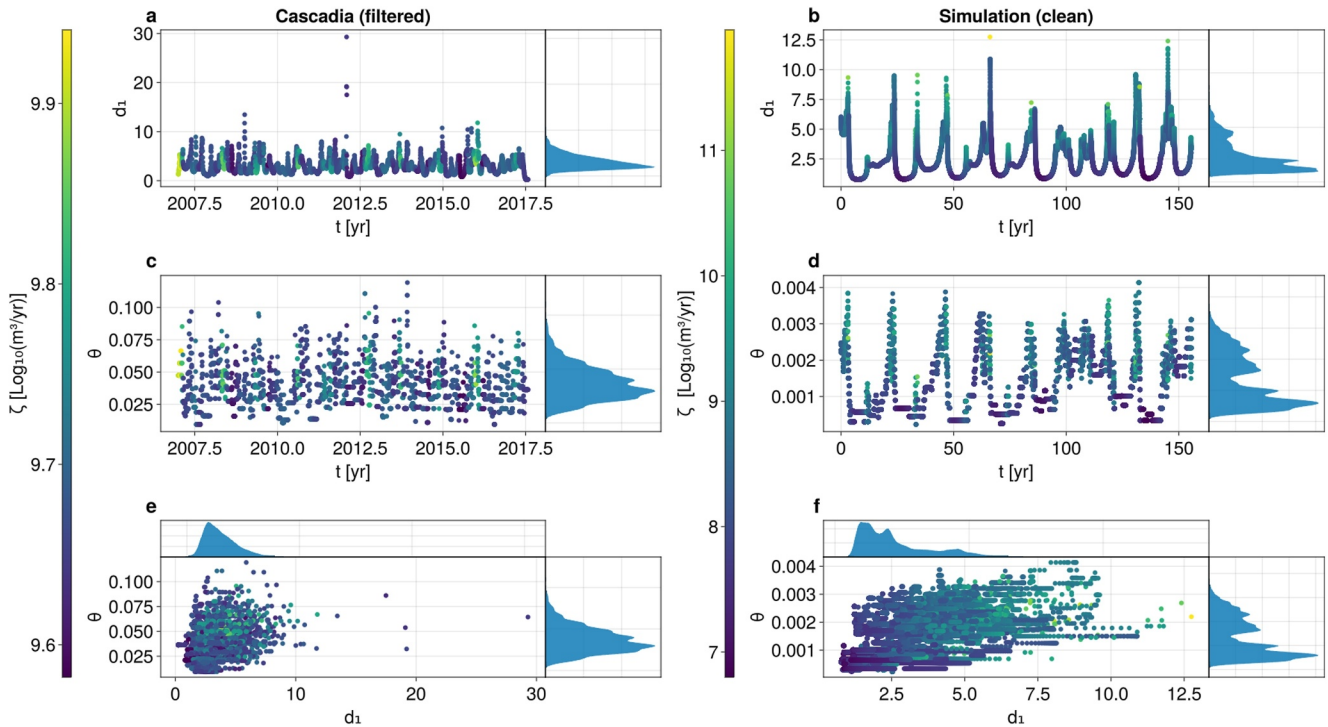atural slow earthquake data and might provide valuable information to determine when the system is approaching a critical transition, that is, moving from a system scale loading phase to a slipping one and vice-versa. This is particularly true for Cascadia, where d_1 reaches maximum values at the start and at the end of the slip event (i.e., before and after the peaking in slip rate). This peculiar behavior is not ascribable to the filtering procedure because it does not appear in the results relative to the filtered simulations (Figure S7 in Supporting Information S1).

3.2. Time-Averaged Metrics λ_{max} and H_{sp}

The analysis of λ_{max} reveals a behavior similar to the one highlighted for chaotic dynamics (Parlitz, 2016). It involves an initial phase where trajectories converge toward the direction of maximum expansion before revealing exponential divergence, visualized as a linear segment in the semi-logarithmic plot (Figure 4). When the trajectories of the neighbors continue to evolve, a plateau in the distance emerges. The λ_{max} value, derived from the slope of the best linear fit in this scaling region, is displayed atop the respective panels. Once the direction of maximal expansion is reached, there is little influence on the asymptotic estimate of $\lambda_{\text{max}}^{\text{sim}}$ ($0.000674 \pm 0.000008 \text{ d}^{-1}$ and $0.00061 \pm 0.00002 \text{ d}^{-1}$ for clean and noisy simulated time series, respectively, see Figure 4 and Figure S9 in Supporting Information S1).

The values of λ_{max} correspond to Lyapunov times of ~ 43 d and ~ 4.1 yr for Cascadia and the simulated time series, respectively. This discrepancy may be attributed to the difference in inter-event times between the data sets. The

Figure 2. Left: Cascadia. Right: Numerical simulations, respectively. Top row (panels a and b): time evolution of the instantaneous dimension d_1. On the right side of each panel the probability density function. Central row (panels c and d): same as top row, but for the extremal index θ. Bottom row (panels e and f): instantaneous dimension-extremal index space. All panels are color coded by the variable used for the calculation of the dynamical indices, that is, Log_{10} of the slip potency rate.

slow earthquakes are separated by few months in Cascadia and by several years for the numerical simulations. As a consequence, two nearby trajectories in the simulations may spend more time in the almost linear inter-event regime, giving a larger Lyapunov time. Nonetheless, we retrieve a positive $\lambda_{\max}$ for the spatio-temporally
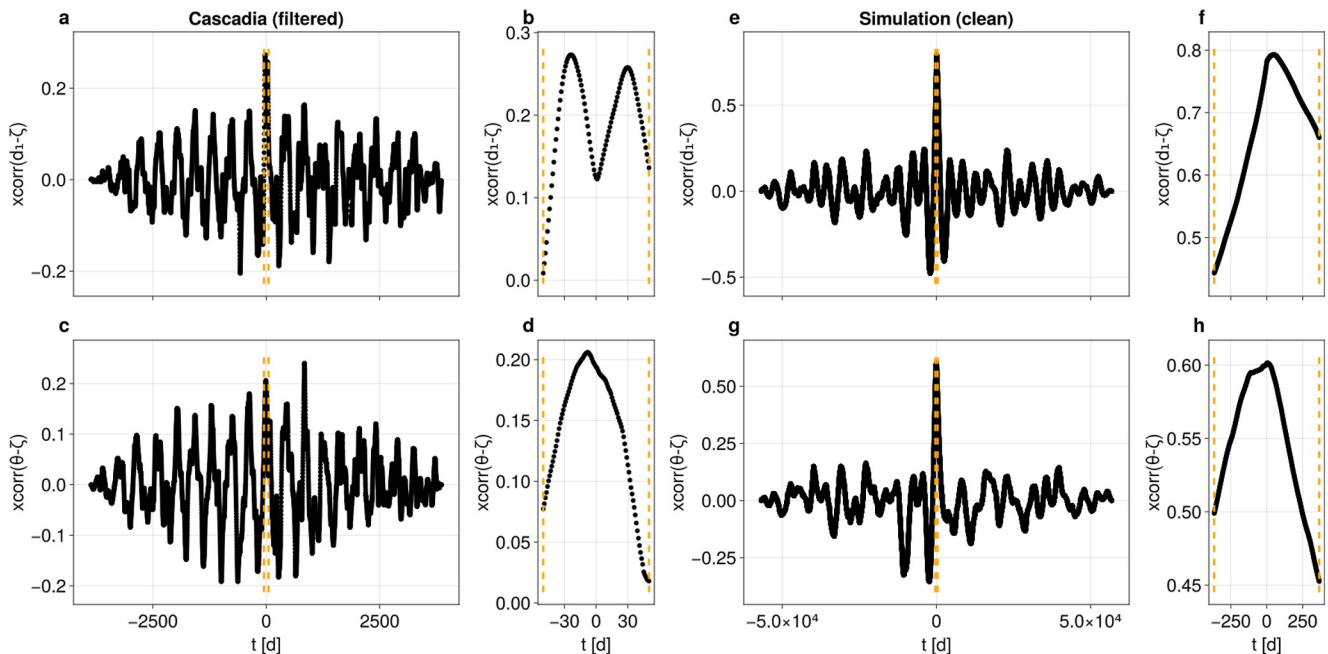

Figure 3. Left: Cascadia. Right: Numerical simulations. Top row (panels a–b and e–f): normalized cross-correlation between d_1 and the observable ζ calculated as the Log_{10} of the slip potency rate integrated over the whole slipping region. Bottom row (panels c–d and g–h): Same as top row, but using the local index θ.
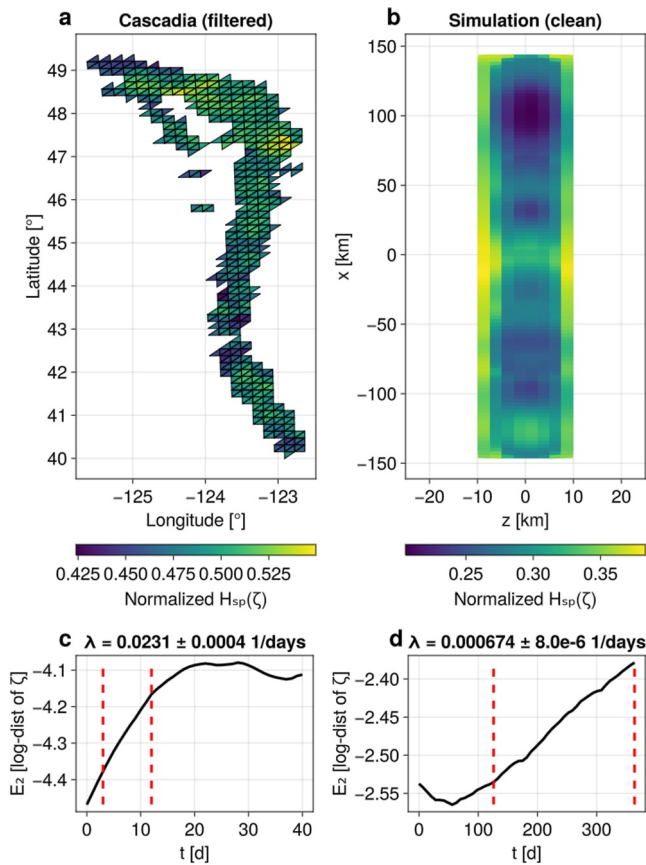
Figure 4. Left: Cascsadia. Right: Numerical simulations. Top row (panels a and b): Normalized spectral entropy for every time series associated with a slipping patch. Bottom row (panels c and d): Log-distance E_2 evolution with number of time steps. Red dashed line indicate the scaling region considered for the estimation of $\lambda_{\max}$.

coarsened numerical simulations, also in the clean case. We calculated $\lambda_{\max}$ for periodic daily time series with 1 year period, obtaining no positive values: the sensitivity to initial conditions is not dictated by the temporal coarsening, but is likely a characteristic of the system under study.

To compare the differences in the degree of complexity between the natural and simulated cases, we also calculate the normalized spectral entropy, H_{sp}, depicted in Figure 4. It is computed for the time series corresponding to each patch, showcasing the spatial variability of H_{sp}, with Cascadia results on the left and numerical simulation outcomes on the right. We also calculate H_{sp} for periodic signals (with 1 year period and randomized initial phase) and normally distributed noise for a number of time series equal to the number of patches of the two data sets. These signals should have H_{sp} equal to 0 and 1, respectively. This calculation provides an expected value and a standard deviation given the temporal sampling and number of available points. We obtain $H_{sp}^{periodic} = 0.195 \pm 0.003$ and $H_{sp}^{randn} = 0.944 \pm 0.002$ for the seasonal and random signal for the Cascadia conditions, and $H_{sp}^{periodic} = 0.1361 \pm 0.0001$ and $H_{sp}^{randn} = 0.9585 \pm 0.0003$ for the simulated data set. This means that the daily temporal sampling is likely partially masking the true nature of a periodic signal, resulting in a non-null spectral entropy. Moreover, for random time series the normalized spectral entropy is slightly smaller than unity, likely because of the finite length of the available time series. The results obtained for Cascadia and simulated SSEs clearly fall in the between of these two categories, showing once more the aperiodic but not purely random nature of this phenomenon.

4. Discussions

The predictability horizon, estimated as the inverse of the maximum Lyapunov exponent $\lambda_{\max}$, is an average, asymptotic quantity. When predicting an extreme event, like a slow earthquake, we are interested in the instantaneous predictability of the system, and not just its average asymptotic behavior. The local (or instantaneous) extramal index θ shows lower values (i.e., longer persistence and, likely, higher predictability) during the inter-event time, where the dynamics could be linearly approximated. This is the case when using the slip potency rate or its logarithm, but if we use directly the slip potency as input variable we observe low values of θ during the pre- and post-SSEs periods (Figure 2 and Figure S6 in Supporting Information S1). It is known that the selection of the variable under exam can affect the retrieved dynamical indices of the system (e.g., Lorenz, 1991). Future investigations will be focused on a detailed sensitivity analysis on how the local indices vary depending on the selected input variable.

Here we focused on the effects induced by corrupting numerical simulations in such a way to reproduce conditions available from real-world data. The increase of about one order of magnitude in $\theta^{\max}$ when we corrupt and filter the numerical simulations indicates that this disturbance is the primary cause of uncertainty for short-term predictions of the system. If we were converting the information on θ into a predictability horizon, we would get a minimum value of about 241 d for clean numerical simulations, and this would reduce to about 34 d after filtering the noisy simulations. For Cascadia the minimum predictability horizon is estimated to be about 5 d, similar to what obtained studying the slipping segments individually (Gualandi, Avouac, et al., 2020). This value is about one order of magnitude smaller than the predictability horizon of ~43 d obtained from $\lambda_{\max}$. Similar values (30 − 45 d) were recently obtained estimating $\lambda_{\max}$ from displacement GNSS time series in New Zealand under the assumption that the observed displacement can be ascribed to fault slip (Truttmann et al., 2024). In the same work, the correlation dimension, which is another asymptotic property of the attractor, has been calculated, obtaining values smaller than five. We want to remark here the importance of getting instantaneous information about the system, because the asymptotic behavior of the system may be of limited practical utility when dealing with extreme events.

It is also important to notice that the Lyapunov exponent that we have calculated has been retrieved after a spatio-temporal coarsening of the true simulations. Deterministic non-chaotic time series with coarsened temporal resolution could give rise to positive λ_{max} (e.g., Gualandi et al., 2023). In practice, we have estimated all the proposed metrics at a mesoscopic scale. It is possible that at a miscroscopic scale the unpredictability is even stronger, with larger Lyapunov exponents (Falasco et al., 2015). Even if we are unable to assess the nucleation phase in its microscopical details at the current spatio-temporal resolution, we still may be able to attempt forecasts of the large-scale behavior. This is similar to weather analysis, where the maximum Lyapunov exponents associated with eddies of boundary layer turbulence provide predictability horizons of fractions of a second, but this does not prevent reliable forecasts up to several hours (Siegert & Kantz, 2016). Given the detrimental effect of observational noise on the estimated predictability horizon, we think that an area of research to further develop is the one focused on better extracting the tectonic signal from geodetic GNSS time series (e.g., Costantino et al., 2023).

Both real-world and simulated data exhibit chaotic characteristics, with exponential divergence of nearby trajectories (Figure 4) and a fractional average dimension. The simulations here considered are fully deterministic, but the nature of this chaotic behavior in real-world data, deterministic (as in the classic Lorenz63 system (Lorenz, 1963)) or stochastic (as in random attractors (Crauel et al., 1997; Faranda, Sato, et al., 2017; Gualandi et al., 2023)), is not clear. On the one hand, the low-average dimension suggests that a reduced order model might be suitable to describe the system. On the other hand, high instantaneous dimensions indicate that extra dof, likely corresponding to fast dynamical modes or small-scale perturbations, must be accounted for either with a high-dimensional deterministic system or by a low-dimensional stochastic system. Real-world faults are clearly affected by stress redistribution due, for example, to static and dynamic stress transfer induced by nearby or far earthquakes (e.g., Belardinelli et al., 2003; King et al., 1994), post-seismic relaxation processes (e.g., Gualandi, Liu, & Rollins, 2020; Perfettini & Avouac, 2004), SSEs (e.g., Radiguet et al., 2016), rainfall (e.g., Hainzl et al., 2006; D'Agostino et al., 2018; Pintori et al., 2021), volcanic activity (e.g., Chen et al., 2019), human activity (e.g., Smith et al., 2019). For the particular case of slow earthquakes, these can be affected also by ocean and solid tides (e.g., Hawthorne & Rubin, 2010; Rubinstein et al., 2008). Because of the lack of detailed knowledge of the stress perturbations, Stochastic Differential Equations (SDE) might be a more suitable framework to describe a complex phenomenon like frictional sliding in nature (Gualandi et al., 2023; Matthews et al., 2002), allowing us to consider the effect of these extra dof. SOC suggests that earthquake unpredictability is caused by critical fluctuations due to infinite many dof rather than a low-dimensional chaotic behavior of the system (Bak & Tang, 1989). Here we have shown that the existence of many dof (i.e., $d_1^{max} > 10$) can be reconciled with a small average dimension ($D_1 < 5$), contributing to the debate about the possible interpretation of earthquakes as a SOC phenomenon or not (Main, 1999; Main & Naylor, 2008). Future developments will aim at finding features that can enable us to distinguish between the two aforementioned possibilities to enact complex behavior (deterministic high-dimensional ODE/PDE on the one hand and low-dimensional SDE on the other hand).

We tested the effect of observational noise on the retrieved dynamical indices. For the estimate of λ_{max}, noisy time series reach the scaling region in the E_2 graph in more than 200 d (Figure S9 in Supporting Information S1), that is, more slowly with respect to the noise-free case (less than 150 d, Figure 4, panel d). Moreover, the log-distances are smaller if compared to noise-free time series, an effect that might be due to the filtering procedure. Observational noise distorts the estimated indices, but is not sufficient to explain the higher complexity of natural slow earthquakes. To further characterize the complexity of the system we used the power spectral entropy (Llanos et al., 2017). Cascadia time series have H_{sp} larger than the simulations, indicating a less periodic-like behavior. The addition of noise brings the maximum H_{sp} for simulations at values similar to the minimum of Cascadia, suggesting that some complexity in the natural case is still not captured. The values obtained are clearly in between a fully periodic system and a completely random process. Figure 4 reveals an intriguing feature for simulated data: the regions with lower H_{sp} are those where SSEs tend to nucleate. For Cascadia, low H_{sp} is either at the edges of the fault or where fault strike varies. It is well known that fault complexities can result in heterogeneous stress fields and complex interactions among various segments (e.g., Cattania, 2019; Romanet et al., 2018). H_{sp} might offer a way to determine the resulting segmentation, for instance by connecting the blue regions (low values of H_{sp}) in Figure 4.

In all cases, we found $d_1^{max} > 10$. This high local dimensionality is likely due to the nature of the system, which is complex and with interactions among many of its parts. This is another way in which the observed segmentation is

likely manifesting, suggesting that the measured dimensions might be representative of a sub-system, coupled with other subsystems at different spatio-temporal scales (e.g., Tsonis & Elsner, 1988). However, the causes of the segmentation between Cascadia and simulations seem to have different origins. For the natural case we discussed how the stress field could be continuously externally perturbed. When numerical simulations of the seismic cycle are properly extended to the continuum limit, it is common to observe periodic behavior (Rice, 1993). For the simulated case the perturbation took place at the beginning, assigning a random stress field that generated the heterogeneity necessary to develop the segmentation. This difference is subtle, but not irrelevant. Indeed, the perturbations applied should not be frozen in time (i.e., applied only to the initial condition), but evolve.

In conclusion, this study provides new insights into the chaotic behaviors and dynamic complexities of slow earthquakes and a stride toward more accurate slow earthquake forecasting and modeling. The comparison between sophisticated numerical simulations and real-world data has pinpointed areas requiring further refinement in our modeling approaches. To enhance the predictive accuracy and reliability of earthquake models, it is pivotal to reduce observational noise and integrate evolving stress perturbations. Furthermore, the exploration of ensemble forecasting and the incorporation of kinematic information into seismic cycle predictions are crucial future endeavors.

Data Availability Statement

The data and code are available on Zenodo (Gualandi et al., 2024). Calculations have been performed modifying the library `NonlinearDynamics.jl` (Datseris, 2018; Datseris & Parlitz, 2022).

References

Bak, P., & Tang, C. (1989). Earthquakes as a self-organized critical phenomenon. *Journal of Geophysical Research*, *94*(B11), 15635–15637. https://doi.org/10.1029/jb094ib11p15635

Becker, T. (2000). *Deterministic chaos in two state-variable friction sliders and the effects of elastic interactions*. AGU.

Belardinelli, M., Bizzarri, A., & Cocco, M. (2003). Earthquake triggering by static and dynamic stress changes. *Journal of Geophysical Research*, *108*(B3), 2135. https://doi.org/10.1029/2002JB001779

Ben-Zion, Y. (2008). Collective behavior of earthquakes and faults: Continuum-discrete transitions, progressive evolutionary changes, and different dynamic regimes. *Reviews of Geophysics*, *46*(4006). https://doi.org/10.1029/2008rg000260

Cao, L. (1997). Practical method for determining the minimum embedding dimension of a scalar time series. *Physica D*, *110*(1–2), 43–50. https://doi.org/10.1016/s0167-2789(97)00118-8

Cattania, C. (2019). Complex earthquake sequences on simple faults. *Geophysical Research Letters*, *46*(17–18), 10384–10393. https://doi.org/10.1029/2019GL083628

Chartrand, R. (2011). Numerical differentiation of noisy, nonsmooth data. *ISRN Applied Mathematics*, *2011*(164564), 1–11. https://doi.org/10.5402/2011/164564

Chen, K., Smith, J., Avouac, J., Liu, Z., Song, Y., & Gualandi, A. (2019). Triggering of the Mw 7.2 Hawaii earthquake of 4 May 2018 by a dike intrusion. *Geophysical Research Letters*, *46*(5), 2503–2510. https://doi.org/10.1029/2018GL081428

Costantino, G., Giffard-Roisin, S., Radiguet, M., Dalla Mura, M., Marsan, D., & Socquet, A. (2023). Slow slip detection with deep learning in multi-station raw geodetic time series validated against tremors in cascadia. https://doi.org/10.48550/arXiv.2305.19720

Crauel, H., Debussche, A., & Flandoli, F. (1997). Random attractors. *Journal of Dynamics and Differential Equations*, *9*(2), 307–341. https://doi.org/10.1007/bf02219225

D'Agostino, N., Silverii, F., Amoroso, O., Convertito, V., Fiorillo, F., Ventafridda, G., & Zollo, A. (2018). Crustal deformation andseismicity modulated by groundwaterrecharge of karst aquifers. *Journal of Geophysical Research: Solid Earth*, *45*(22), 12253–12262. https://doi.org/10.1029/2018GL079794

Dal Zilio, L., Lapusta, N., & Avouac, J.-P. (2020). Unraveling scaling properties of slow-slip events. *Geophysical Research Letters*, *47*(10), e2020GL087477. https://doi.org/10.1029/2020GL08747

Dal Zilio, L., van Dinther, Y., Gerya, T., & Avouac, J.-P. (2019). Bimodal seismicity in the Himalaya controlled by fault friction and geometry. *Nature Communications*, *10*(48), 48. https://doi.org/10.1038/s41467-018-07874-8

Datseris, G. (2018). Dynamicalsystems.jl: A julia software library for chaos and nonlinear dynamics [Software]. *Journal of Open Source Software*, *3*(23), 598. https://doi.org/10.21105/joss.00598

Datseris, G., & Parlitz, U. (2022). Nonlinear dynamics: A concise introduction interlaced with code [Software]. *Springer Nature*. https://doi.org/10.1007/978-3-030-91032-7

Day, S., Dalguer, L., Lapusta, N., & Liu, Y. (2005). Comparison of finite difference and boundary integral solutions to three-dimensional spontaneous rupture. *Journal of Geophysical Research*, *110*(B12307). https://doi.org/10.1029/2005JB003813

Dieterich, J. (1979). Modeling of rock friction, 1, experimental results and constitutive equations. *Journal of Geophysical Research*, *8*(B5), 2161–2168. https://doi.org/10.1029/jb084ib05p02161

Falasco, G., Saggiorato, G., & Vulpiani, A. (2015). About the role of chaos and coarse graining in statistical mechanics. *Physics*, *418*, 94–104. https://doi.org/10.1016/j.physa.2014.05.030

Faranda, D., Messori, G., & Yiou, P. (2017). Dynamical proxies of north Atlantic predictability and extremes. *Scientific Reports*, *7*(41278), 41278. https://doi.org/10.1038/srep41278

Faranda, D., Sato, Y., Saint-Michel, B., Wiertel, C., Padilla, V., Dubrulle, B., & Daviaud, F. (2017). Stochastic chaos in a turbulent swirling flow. *Physical Review Letters*, *119*(1), 014502. https://doi.org/10.1103/PhysRevLett.119.014502

Gomberg, J., Belardinelli, M., Cocco, M., & Reasenberg, P. (2005). Time-dependent earthquake probabilities. *Journal of Geophysical Research*, *110*(B05S04). https://doi.org/10.1029/2004JB003405

Grassberger, P., & Procaccia, I. (1983). Measuring the strangeness of strange attractors. *Physica D*, *9*(189), 189–208. https://doi.org/10.1016/0167-2789(83)90298-1

Gualandi, A., Avouac, J.-P., Michel, S., & Faranda, D. (2020). The predictable chaos of slow earthquakes. *Science Advances*, *6*(27). https://doi.org/10.1126/sciadv.aaz5548

Gualandi, A., Dal Zilio, L., Faranda, D., & Mengaldo, G. (2024). Similarities and differences between natural and simulated slow earthquakes - Data and Software (v1.0) [Software]. *Zenodo*. https://doi.org/10.5281/zenodo.12571984

Gualandi, A., Faranda, D., Marone, C., Cocco, M., & Mengaldo, G. (2023). Deterministic and stochastic chaos characterize laboratory earthquakes. *Earth and Planetary Science Letters*, *604*(117995), 117995. https://doi.org/10.1016/j.epsl.2023.117995

Gualandi, A., Liu, Z., & Rollins, C. (2020). Post-large earthquake seismic activities mediated by aseismic deformation processes. *Earth and Planetary Science Letters*, *530*, 115870. https://doi.org/10.1016/j.epsl.2019.115870

Gualandi, A., Nichele, C., Serpelloni, E., Chiaraluce, L., Anderlini, L., Latorre, D., et al. (2017). Aseismic deformation associated with an earthquake swarm in the northern Apennines (Italy). *Geophysical Research Letters*, *44*(15), 7706–7714. https://doi.org/10.1002/2017gl073687

Hainzl, S., Kraft, T., Wassermann, J., Igel, H., & Schmedes, E. (2006). Evidence for rainfall-triggered earthquake activity. *Geophysical Research Letters*, *33*(L19303). https://doi.org/10.1029/2006GL027642

Hawthorne, J., & Rubin, A. (2010). Tidal modulation of slow slip in Cascadia. *Journal of Geophysical Research*, *115*(B09406). https://doi.org/10.1029/2010JB007502

Huang, J., & Turcotte, D. L. (1990). Evidence for chaotic fault inter-actions in the seismicity of the San Andreas Fault and Nankai trough. *Nature*, *348*(6298), 234–236. https://doi.org/10.1038/348234a0

Johanson, I. A., Fielding, E. J., Rolandone, F., & Bürgmann, R. (2006). Coseismic and postseismic slip of the 2004 parkfield earthquake from space-geodetic data. *Bulletin of the Seismological Society of America*, *96*(4B), S269–S282. https://doi.org/10.1785/0120050818

Kano, M., Aso, N., Matsuzawa, T., Ide, S., Annoura, S., Arai, R., et al. (2018). Development of a slow earthquake database. *Seismological Research Letters*, *89*(4), 1566–1575. https://doi.org/10.1785/0220180021

King, G., Stein, R., & Lin, J. (1994). Static stress changes and the triggering of earthquakes. *Bulletin of the Seismological Society of America*, *84*(3), 935–953. https://doi.org/10.1785/BSSA0840030935

Lapusta, N., & Liu, Y. (2009). Three-dimensional boundary integral modeling of spontaneous earthquake sequences and aseismic slip. *Journal of Geophysical Research*, *114*(B09303). https://doi.org/10.1029/2008JB005934

Lapusta, N., Rice, J., Ben-Zion, Y., & Zheng, G. (2000). Elastodynamic analysis for slow tectonic loading with spontaneous rupture episodes on faults with rate- and state-dependent friction. *Journal of Geophysical Research*, *105*(B10), 23765–23789. https://doi.org/10.1029/2000JB900250

Leeman, J., Marone, C., & Saffer, D. (2018). Frictional mechanics of slow earthquakes. *Journal of Geophysical Research: Solid Earth*, *123*(9), 7931–7949. https://doi.org/10.1029/2018JB015768

Llanos, F., Alexander, J., Stilp, C., & Kluender, K. (2017). Power spectral entropy as an information-theoretic correlate of manner of articulation in American English. *Journal of the Acoustical Society of America*, *141*(2), EL127–EL133. https://doi.org/10.1121/1.4976109

Lorenz, E. (1963). Deterministic nonperiodic flow. *Journal of the Atmospheric Sciences*, *20*(2), 130–141. https://doi.org/10.1175/1520-0469(1963)020<0130:dnf>2.0.co;2

Lorenz, E. (1991). Dimension of weather and climate attractors. *Nature*, *353*(6341), 241–244. https://doi.org/10.1038/353241a0

Main, I. (1996). Statistical physics, seismogenesis, and seismic hazard. *Review of Geophysics*, *34*(4), 433–462. https://doi.org/10.1029/96RG02808

Main, I. (1999). Earthquake prediction: Concluding remarks. *Nature*. https://doi.org/10.1038/nature28133

Main, I., & Naylor, M. (2008). Maximum entropy production and earthquake dynamics. *Geophysical Research Letters*, *35*(L19311). https://doi.org/10.1029/2008GL035590

Matthews, M., Ellsworth, W., & Reasenberg, P. (2002). A Brownian model for recurrent earthquakes. *Bulletin of the Seismological Society of America*, *92*(6), 2233–2250. https://doi.org/10.1785/0120010267

McCloskey, J., & Bean, C. (1992). Time and magnitude predictions in shocks due to chaotic fault interactions. *Geophysical Research Letters*, *19*(2), 119–122. https://doi.org/10.1029/92GL00099

Michel, S., Gualandi, A., & Avouac, J.-P. (2019a). Interseismic coupling and slow slip events on the Cascadia megathrust. *Pure and Applied Geophysics*, *176*(9), 3867–3891. https://doi.org/10.1007/s00024-018-1991-x

Michel, S., Gualandi, A., & Avouac, J.-P. (2019b). Similar scaling laws for earthquakes and Cascadia slow-slip events. *Nature*, *574*(7779), 522–526. https://doi.org/10.1038/s41586-019-1673-6

Parlitz, U. (2016). *Estimating Lyapunov exponents from time series* (1st ed.). Springer International Publishing.

Perfettini, H., & Avouac, J.-P. (2004). Postseismic relaxation driven by brittle creep: A possible mechanism to reconcile geodetic measurements and the decay rate of aftershocks, application to the Chi-Chi earthquake, Taiwan. *Journal of Geophysical Research*, *109*(B02304). https://doi.org/10.1029/2003JB002488

Philibosian, B., & Meltzner, A. (2020). Segmentation and supercycles: A catalog of earthquake rupture patterns from the Sumatran Sunda megathrust and other well-studied faults worldwide. *Quaternary Science Reviews*, *241*, 106390. https://doi.org/10.1016/j.quascirev.2020.106390

Pintori, F., Serpelloni, E., Longuevergne, L., Garcia, A., Faenza, L., D'Alberto, L., et al. (2021). Mechanical response of shallow crust to groundwater storage variations: Inferences from deformation and seismic observations in the eastern Southern Alps, Italy. *Journal of Geophysical Research: Solid Earth*, *126*(2). https://doi.org/10.1029/2020JB020586

Radiguet, M., Cotton, F., Vergnolle, M., Campillo, M., Walpersdorf, A., Cotte, N., & Kostoglodov, V. (2012). Slow slip events and strain accumulation in the Guerrero Gap, Mexico. *Journal of Geophysical Research*, *117*(B04305). https://doi.org/10.1029/2011JB008801

Radiguet, M., Perfettini, H., Cotte, N., Gualandi, A., Valette, B., Kostoglodov, V., et al. (2016). Triggering of the 2014 Mw7.3 Papanoa earthquake by a slow slip event in Guerrero, Mexico. *Nature Geoscience*, *9*(11), 829–833. https://doi.org/10.1038/ngeo2817

Rice, J. (1993). Spatio-temporal complexity of slip on a fault. *Journal of Geophysical Research*, *98*(B6), 9885–9907. https://doi.org/10.1029/93jb00191

Rice, J., & Ruina, L. (1983). Stability of steady frictional slipping. *Journal of Applied Mechanics*, *50*(2), 343–349. https://doi.org/10.1115/1.3167042

Romanet, P., Bhat, H., Jolivet, R., & Madariaga, R. (2018). Fast and slow slip events emerge due to fault geometrical complexity. *Geophysical Research Letters*, *45*(10), 4809–4819. https://doi.org/10.1029/2018GL077579

Rosenau, M., Corbi, F., & Dominguez, S. (2017). Analogue earthquakes and seismic cycles: Experimental modelling across timescales. *Solid Earth*, *8*(3), 597–635. https://doi.org/10.5194/se-8-597-2017

Rubinstein, J., La Rocca, M., Vidale, J., Creager, K., & Wech, A. (2008). Tidal modulation of nonvolcanic tremor. *Science*, *319*(5860), 186–189. https://doi.org/10.1126/science.1150558

Ruina, L. (1983). Slip instability and state variable friction laws. *Journal of Geophysical Research*, *88*(B12), 10359–10370. https://doi.org/10.1029/jb088ib12p10359

Sano, M., & Sawada, Y. (1985). Measurement of the Lyapunov spectrum from a chaotic time series. *Physical Review Letters*, *55*(10), 1082–1085. https://doi.org/10.1103/physrevlett.55.1082

Schwartz, S., & Rokosky, J. (2007). Slow slip events and seismic tremor at circum-Pacific subduction zones. *Reviews of Geophysics*, *45*(RG3004). https://doi.org/10.1029/2006RG000208

Segall, P., & Rice, J. (1995). Dilatancy, compaction, and slip instability of a fluid-infiltrated fault. *Journal of Geophysical Research*, *100*(B11), 22155–22171. https://doi.org/10.1029/95jb02403

Siegert, S., & Kantz, H. (2016). *Prediction of complex dynamics: Who cares about chaos?* (1st ed.). Springer International Publishing.

Smith, J., Avouac, J.-P., White, R., Copley, A., Gualandi, A., & Bourne, S. (2019). Reconciling the long-term relationship between reservoir pore pressure depletion and compaction in the Groningen region. *Journal of Geophysical Research: Solid Earth*, *124*(6), 6165–6178. https://doi.org/10.1029/2018JB016801

Tinti, E., Scuderi, M., Scognamiglio, L., Di Stefano, G., Marone, C., & Collettini, C. (2016). On the evolution of elastic properties during laboratory stick-slip experiments spanning the transition from slow slip to dynamic rupture. *Journal of Geophysical Research: Solid Earth*, *121*(12), 8569–8594. https://doi.org/10.1002/2016JB013545

Truttmann, S., Poulet, T., Wallace, L., Herwegh, M., & Veveakis, M. (2024). Slow slip events in New Zealand: Irregular, yet predictable? *Geophysical Research Letters*, *51*(6), e2023GL107741. https://doi.org/10.1029/2023GL107741

Tsonis, A., & Elsner, J. (1988). The weather attractor over very short timescales. *Nature*, *333*(9), 545–547. https://doi.org/10.1038/333545a0

Voss, N., Dixon, T., Liu, Z., Malservisi, R., Protti, M., & Schwartz, S. (2018). Do slow slip events trigger large and great megathrust earthquakes? *Science Advances*, *4*(eaat8472). https://doi.org/10.1126/sciadv.aat8472

Wolf, A., Swift, J., Swinney, H., & Vastano, J. (1985). Determining Lyapunov exponents from a time series. *Physica D: Nonlinear Phenomena*, *16*(3), 285–317. https://doi.org/10.1016/0167-2789(85)90011-9

References From the Supporting Information

Alberti, T., De Michelis, P., Santarelli, L., Faranda, D., Consolini, G., & Marcucci, M. F. (2023). Tracking geomagnetic storms with dynamical system approach: Ground-based observations. *Remote Sensing*, *15*(3031), 3031. https://doi.org/10.3390/rs15123031

Benettin, G., Galgani, A., Giorgilli, A., & Strelcyn, J.-M. (1980). Lyapunov characteristic exponents for smooth dynamical systems and for Hamiltonian systems: A method for computing all of them. Part 2: Numerical application. *Meccanica*, *15*(21), 21–30. https://doi.org/10.1007/bf02128237

Faranda, D., & Vaienti, S. (2018). Correlation dimension and phase space contraction via extreme value theory. *Chaos*, *28*(4), 041103. https://doi.org/10.1063/1.5027386

Lucarini, V., Faranda, D., Freitas, A. C. M., Freitas, J. M., Holland, M., Kuna, T., et al. (2016). *Extremes and recurrence in dynamical systems* (1st ed.). Wiley.

Moloney, N. R., Faranda, D., & Sato, Y. (2019). An overview of the extremal index. *Chaos*, *29*(2), 022101. https://doi.org/10.1063/1.5079656

Shannon, C. E. (1949). Communication theory of secrecy systems. *Bell System Technical Journal*, *28*(4), 656–715. https://doi.org/10.1002/j.1538-7305.1949.tb00928.x

Shimada, I., & Nagashima, T. (1979). A numerical approach to ergodic problem of dissipative dynamical systems. *Progress of Theoretical Physics*, *61*(6), 1605–1616. https://doi.org/10.1143/ptp.61.1605

Theiler, J. (1986). Spurious dimension from correlation algorithms applied to limited time-series data. *Physical Review*, *34*(3), 2427–2432. https://doi.org/10.1103/physreva.34.2427